THE ASTROPHYSICAL JOURNAL, IN PRESS, AUGUST 8, 2023
Typeset using LaTeX **twocolumn** style in AASTeX631

Magnetohydrodynamic Mode Conversion in the Solar Corona: Insights from Fresnel-like Models of Waves at Sharp Interfaces

STEVEN R. CRANMER[1] AND MOMCHIL E. MOLNAR[1,2,3]

[1]*Department of Astrophysical and Planetary Sciences, Laboratory for Atmospheric and Space Physics, University of Colorado, Boulder, CO, USA*
[2]*National Solar Observatory, Boulder, CO, USA*
[3]*High Altitude Observatory, National Center for Atmospheric Research, Boulder, CO, USA*

ABSTRACT

The solar atmosphere is known to contain many different types of wavelike oscillation. Waves and other fluctuations (e.g., turbulent eddies) are believed to be responsible for at least some of the energy transport and dissipation that heats the corona and accelerates the solar wind. Thus, it is important to understand the behavior of magnetohydrodynamic (MHD) waves as they propagate and evolve in different regions of the Sun's atmosphere. In this paper, we investigate how MHD waves can affect the overall plasma state when they reflect and refract at sharp, planar interfaces in density. First, we correct an error in a foundational paper (Stein 1971) that affects the calculation of wave energy-flux conservation. Second, we apply this model to reflection-driven MHD turbulence in the solar wind, where the presence of density fluctuations can enhance the generation of inward-propagating Alfvén waves. This model reproduces the time-averaged Elsasser imbalance fraction (i.e., ratio of inward to outward Alfvénic power) from several published numerical simulations. Lastly, we model how the complex magnetic field threading the transition region between the chromosphere and corona helps convert a fraction of upward-propagating Alfvén waves into fast-mode and slow-mode MHD waves. These magnetosonic waves dissipate in a narrow region around the transition region and produce a sharp peak in the heating rate. This newly found source of heating sometimes exceeds the expected heating rate from Alfvénic turbulence by an order of magnitude. It may explain why some earlier models seemed to require an additional ad-hoc heat source at this location.

Keywords: Alfvén waves (23) – Interplanetary turbulence (830) – Magnetohydrodynamics (1964) – Solar corona (1483) – Solar coronal heating (1989) – Solar wind (1534)

1. INTRODUCTION

The Sun's photosphere, chromosphere, and corona are highly dynamic, exhibiting stochastic and intermittent variability across many orders of magnitude in space and time. These fluctuations have long been suspected to be important contributors to how the plasma is heated (see, e.g., Aschwanden 2006; Parnell & De Moortel 2012; Fletcher et al. 2015; Van Doorsselaere et al. 2020). Many of the proposed conceptual mechanisms involve oscillating magnetohydrodynamic (MHD) waves. Some propose that convective motions drive oscillations at the solar surface that propagate up to larger heights and then dissipate to provide coronal heating (Alfvén 1947; Spruit 1981; Musielak & Ulmschneider 2002; Cranmer & van Ballegooijen 2005; Jess et al. 2023). Others suggest that the evolving magnetic field triggers isolated bursts of magnetic reconnection that generate wave activity throughout the solar atmosphere (Hollweg 1990; Axford & McKenzie 1992; Kigure et al. 2010; Lynch et al. 2014).

In addition to the relatively straightforward mechanisms described above, there are likely to be many other indirect ways for MHD waves to be generated and to evolve (i.e., to transform their properties as they propagate from one place to another in the solar atmosphere). The literature on both linear and nonlinear *mode conversion* is vast, and we can only provide pointers to a small fraction of it for further study. When the magnetic field strength and other background plasma properties (e.g., density and temperature) vary with position, it allows waves of one type to transform into another (see, e.g., Lee & Roberts 1986; Bogdan et al. 2002; McDougall & Hood 2007; Cally & Goossens 2008; Tarr et al. 2017; Cally 2022; Huang et al. 2022). In addition,

Corresponding author: Steven R. Cranmer

when waves encounter inhomogeneities such as velocity shears, there can arise both linear (Bavassano et al. 1978; Kaghashvili 1999, 2007, 2013; Hollweg & Kaghashvili 2012) and nonlinear (Nakariakov et al. 1998; Bacchini et al. 2022) channels to convert some waves into different modes. In many realistic inhomogeneous environments, the modes themselves become "mixed" and the usual separation into ideal fast, slow, and Alfvén modes is not possible (e.g., Goossens et al. 2019). When MHD waves propagate through random or stochastic background conditions, it can trigger phenomena such as resonances, instabilities, and turbulent cascade (Valley 1971, 1974; Lou & Rosner 1986; Li & Zweibel 1987; Murawski et al. 2001; Yuan et al. 2015; Srivastava et al. 2021; Morton et al. 2023). Lastly, when wave amplitudes become large, there can arise various varieties of shock, soliton, jet, and vortex phenomena that render meaningless the dividing lines between textbook "normal modes" of wavelike oscillation (e.g., Vasquez & Hollweg 1996; Hasan et al. 2003; Ryutova & Hagenaar 2007; Cranmer & Woolsey 2015; Snow et al. 2018).

Despite the dizzying array of proposed mechanisms of MHD wave mode conversion, there are a few that we believe have not received sufficient attention. Specifically, in this paper we examine some of the consequences of a model first discussed by Stein (1971). That paper studied the consequences for a wave obliquely incident on a sharp planar boundary at which the plasma density varies abruptly. In ideal MHD, a wave of one type (i.e., slow-mode, fast-mode, or Alfvénic) produces reflected and transmitted power in waves of all three types. In Section 2, we describe this model in detail and correct an error in one of the equations given by Stein (1971). In Section 3, we apply this model to the solar wind in order to better understand how density fluctuations can enhance the large-scale reflection of imbalanced Alfvénic turbulence. In Section 4, we simulate the Sun's complex "magnetic carpet" in order to see how Alfvén waves incident on the sharp transition region (TR) will naturally transfer some of their energy to both upward and downward propagating fast/slow-mode magnetosonic waves. These compressive waves dissipate very efficiently at the TR, so they appear to provide an added "pulse" of coronal heating that has not been considered before. Lastly, in Section 5, we conclude by summarizing these results, discussing possible future improvements, and suggesting some additional applications of the Stein (1971) theory.

2. REFLECTION AND TRANSMISSION OF MHD WAVES

Here we describe the setup of an idealized MHD system containing a planar discontinuity in the background plasma parameters. We often follow the notation of Stein (1971),

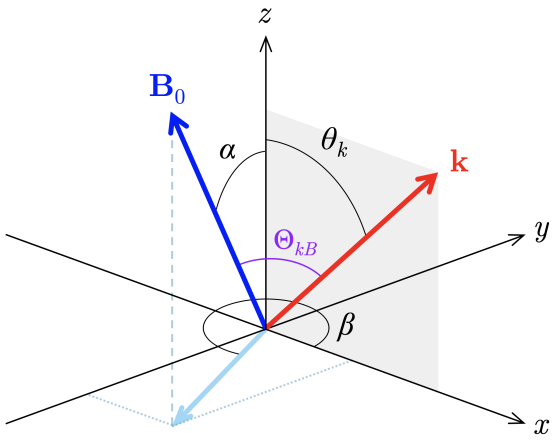

Figure 1. Coordinate system and vectors for the idealized MHD system of wave reflection and transmission. Wavenumber $\mathbf{k}$ (red) always remains in the x-z plane, and it is offset from the z-axis by a polar angle θ_k. Spherical coordinate angles α and β describe the magnetic field vector (blue).

but we also correct an error in one of Stein's equations that led to the normal component of the total wave energy flux to not be conserved. We also take inspiration from additional studies of waves at sharp interfaces such as Vasquez (1990), Terradas et al. (2011), and Vickers et al. (2018), and we anticipate that many of the results discussed below will also be valid for environments where the interface has a *finite* thickness smaller than the other relevant length-scales (e.g., scale heights and wavelengths) of the medium.

We define coordinates such that the discontinuity occurs in the plane described by $z = 0$, and in general the mass density ρ, temperature T, and magnetic field strength B_0 can be different in the two homogenous half-spaces defined by $z < 0$ and $z > 0$. In this work, we choose to keep the both the magnetic field and the background gas pressure ($P_0 \propto \rho T$) constant across the discontinuity. Thus, we specify ρ_1 and T_1 for $z < 0$, and ρ_2 and T_2 for $z > 0$, with

$$\rho_1/\rho_2 = T_2/T_1 \ . \tag{1}$$

Figure 1 illustrates various quantities in the Cartesian coordinate system defined by the discontinuity in the x-y plane. An incident MHD plane-wave travels up from the $z < 0$ region, encounters the discontinuity, and creates a set of transmitted ($z > 0$) and reflected ($z < 0$) waves as a response. Each of those linear waves has its own wavenumber vector $\mathbf{k}$, but they all share the same angular frequency ω.

The angle between $\mathbf{k}$ and the magnetic field vector $\mathbf{B}_0$ is defined as Θ_{kB}, with

$$\cos\Theta_{kB} = \sin\theta_k \sin\alpha \cos\beta + \cos\theta_k \cos\alpha \ . \tag{2}$$

The characteristic speeds of the plasma are defined as

$$V_\mathrm{A} = \frac{B_0}{\sqrt{4\pi\rho_i}} \quad \text{and} \quad c_s = \sqrt{\frac{\gamma P_0}{\rho_i}} \tag{3}$$

for the Alfvén speed and adiabatic sound speed, respectively, with $i = 1, 2$ depending on the region being described. We always used $\gamma = 5/3$, and we also used the ideal-MHD versions of the fast, slow, and Alfvénic dispersion relations that were given for this coordinate system in Equations (3)–(7) of Stein (1971).

In general, all three types of MHD wave modes may be generated above and below the discontinuity. A range of properties must be continuous at the interface, including the frequency ω and the in-plane component of the wavevector k_x. The dispersion relations are then solved for k_z on both sides of the interface. However, Stein (1971) discussed how some combinations of parameters lead to one or both of the resulting fast-mode waves having a purely imaginary normal wavenumber k_z. In these cases, the fast-mode wave is evanescent and has zero energy flux in the direction normal to the discontinuity. However, this mode still needs to be taken into account when solving for the amplitudes at the interface. We used a complex-variable form of LU decomposition (Turing 1948; Anderson et al. 1999) to solve the associated 6×6 linear system for the amplitudes.

Once the dimensionless amplitudes A are known for the reflected and transmitted wave modes, one can compute F_z, the component of energy flux normal to the discontinuity, for each mode. Strictly speaking, all reflected modes must have $F_z < 0$ and both the incident and transmitted modes must have $F_z > 0$. Note that Equation (B4) of Stein (1971) defined the transverse velocity amplitude of Alfvén waves as

$$u_\perp \;=\; A V_\mathrm{A} \left| \hat{\mathbf{e}}_k \times \hat{\mathbf{e}}_B \right| \;=\; A V_\mathrm{A} \sin\Theta_{kB} \;, \tag{4}$$

where $\hat{\mathbf{e}}_k$ and $\hat{\mathbf{e}}_B$ are unit vectors parallel to $\mathbf{k}$ and $\mathbf{B}_0$. However, Equation (B16) of Stein (1971) defined the z-component of the wave energy flux using the definition $A = u_\perp / V_\mathrm{A}$. Using the proper definition above, the corrected expression for the Alfvén-wave flux becomes

$$F_z \;=\; A^2 \rho_0 V_\mathrm{A}^3 \, \cos\alpha \, \sin^2\Theta_{kB} \, \frac{\cos\Theta_{kB}}{|\cos\Theta_{kB}|} \;. \tag{5}$$

The corresponding expressions for fast and slow magnetosonic waves given by Stein (1971) are correct.

Lastly, we define the reflection and transmission coefficients

$$\mathcal{R}_{ij} \;=\; \left| \frac{F_{z,i}(\text{reflected})}{F_{z,j}(\text{incident})} \right| \quad \text{and} \quad \mathcal{T}_{ij} \;=\; \left| \frac{F_{z,i}(\text{transmitted})}{F_{z,j}(\text{incident})} \right| \tag{6}$$

where, in general, the subscript i can be A, F, or S (for any of the three modes generated at the interface) and the subscript j (for the incident wave) is chosen as only one of either A, F, or S. We always verified that the numerical results satisfy

$$\sum_i \left(\mathcal{R}_{ij} + \mathcal{T}_{ij} \right) \;=\; 1 \;, \tag{7}$$

and that the results are independent of the numerical value chosen for the wave frequency ω. Throughout the remainder of this paper, we consider only the case of the incident waves being Alfvénic (i.e., $j = \mathrm{A}$), and we discuss other scenarios in Section 5.

3. ENHANCED REFLECTION OF ALFVÉNIC TURBULENCE

As a first application of the idealized system described above, we would like to better understand the results of numerical simulations that contain both counter-propagating Alfvén waves and stochastic density fluctuations. Investigations of MHD turbulence in the solar corona and solar wind have found that there is more Alfvén-wave reflection when the density fluctuations are stronger (see, e.g., van Ballegooijen & Asgari-Targhi 2016, 2017). Thus, we explore whether it is possible to model this behavior as a series of reflections and transmissions through multiple discontinuities.

3.1. *Alfvén Waves at a Single Interface*

When the angle $\beta = 0$, the background magnetic field vector $\mathbf{B}_0$ lies in the x-z plane defined by the wavevector $\mathbf{k}$ and the normal to the discontinuity. In that case, the 6×6 matrix decouples into a 2×2 matrix for Alfvén waves and a 4×4 matrix for the fast and slow modes. Vasquez (1990) explored this limiting case and discussed the straightforward analytic solution for Alfvén waves,

$$\mathcal{R}_\mathrm{AA} \;=\; \left(\frac{1 - \Delta}{1 + \Delta} \right)^2 \;, \tag{8}$$

where $\Delta = \sqrt{\rho_2 / \rho_1}$. Interestingly, this result is independent of the values of α and θ_k, as well as independent of the background magnetic field strength. Also, it is the same even if the incident wave goes in the other direction through the interface (i.e., if the density jump Δ is replaced by $1/\Delta$).

3.2. *Alfvén Waves at a Multiple Interfaces*

For a system containing multiple interfaces (all assumed to be mutually parallel planes with identical magnitudes Δ), it is possible to determine the net effect of Alfvén-wave transmission and reflection through them. Even for just two interfaces, the total reflection coefficient is the result of an infinite series of reflected waves. Figure 2 illustrates this infinite series. Specifically, the first reflection is immediate. The second is the result of one transmission, then one reflection (at the second interface), then another transmission back toward the source. The third is the result of one transmission, then three "internal bounce" reflections, then another transmission back to the source. The fourth is the result of one transmission, then five reflections, then another transmission, and so

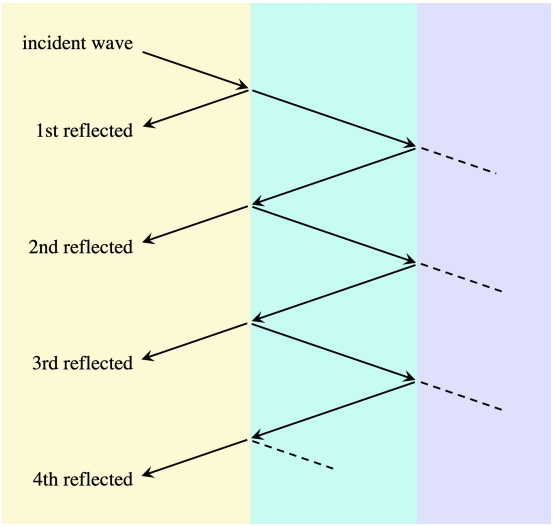

Figure 2. Illustration of how reflection from two parallel interfaces results in an infinite series of reflected components.

on. Using the shorthand notation $\mathcal{R}_1$ for the reflection coefficient given in Equation (8), the total reflection coefficient for two interfaces is given by

$$\mathcal{R}_2 \;=\; \mathcal{R}_1 + \mathcal{T}_1^2 \mathcal{R}_1 \left(1 + \mathcal{R}_1^2 + \mathcal{R}_1^4 + \mathcal{R}_1^6 + \cdots \right) \;. \quad (9)$$

Note that the following infinite series converges,

$$\sum_{n=0}^{\infty} \mathcal{R}_1^{2n} \;=\; \frac{1}{1 - \mathcal{R}_1^2} \quad (10)$$

as long as $|\mathcal{R}_1| < 1$. Thus, given that $\mathcal{T}_1 = 1 - \mathcal{R}_1$ for the interaction at a single discontinuity, the entire expression simplifies to

$$\mathcal{R}_2 \;=\; \frac{2\mathcal{R}_1}{1 + \mathcal{R}_1} \;. \quad (11)$$

This kind of calculation has been generalized to N interfaces, with a general solution given by

$$\mathcal{R}_N \;=\; \frac{N\mathcal{R}_1}{1 + (N-1)\mathcal{R}_1} \;. \quad (12)$$

Note that, in the limit of $N \to \infty$, the total reflection coefficient $\mathcal{R}_N \to 1$.

These results depend on the multiple interfaces being effectively "sharp" in comparison with the length scales of the waves (i.e., wavelengths corresponding to components of $\mathbf{k}$ normal to the interface). It is also likely that the results depend on the interfaces being positioned at least one or more wavelengths apart from one another, rather than being stacked close together. For additional examples of Alfvén-wave reflection and transmission at multiple interfaces, see Hollweg (1984) and De Pontieu et al. (2001).

3.3. *Application to Compressible Fluctuations*

To apply these concepts to simulations of heliospheric turbulence, we need to model a given spatial distribution of density fluctuations as a series of sharp jumps. Thus, given the statistical properties of the fluctuations, the goal is to compute the magnitude Δ for each (presumed identical) jump. If the fluctuations can be approximated as a periodic waveform, with a mean density ρ_0 and variations that extend to $\pm\Delta\rho$ above and below that mean, then

$$\Delta \;=\; \sqrt{\frac{\rho_0 + \Delta\rho}{\rho_0 - \Delta\rho}} \quad (13)$$

as a representative interface ratio. However, for specific waveform shapes, the amplitude $\Delta\rho$ relates to the root-mean squared (rms) density—i.e., the square root of the variance—in different ways. Using $\delta\rho/\rho_0$ for the ratio of the rms to the mean, we can write

$$\Delta \;=\; \sqrt{\frac{1 + (\delta\rho/\rho_0)\sqrt{s}}{1 - (\delta\rho/\rho_0)\sqrt{s}}} \;, \quad (14)$$

where s is a dimensionless shape factor; see, e.g., Equation (38) of Cranmer et al. (2007). For a square-wave train, $s = 1$. For a sinusoidal wave, $s = 2$. For a sawtooth or triangular waveform, $s = 3$.

Figure 3(a) shows the results of using all three values of s to predict the reflection from a single interface. In this case, the plotted quantity is the ratio of inward to outward Elsasser (1950) amplitudes, which is often specified for simulations of imbalanced MHD turbulence. Here, we associate this ratio with the reflection coefficient as

$$\frac{Z_-}{Z_+} \;=\; \sqrt{\mathcal{R}_1} \;. \quad (15)$$

We also note that the Alfvén speed appears in the definitions of $Z_\pm$, and we presume that the unperturbed density ρ_0 is used in these definitions. In the limit of weak density fluctuations, this gives

$$\frac{Z_-}{Z_+} \;\approx\; \frac{\sqrt{s}}{2} \left(\frac{\delta\rho}{\rho_0} \right) \;. \quad (16)$$

For simplicity, we use $s = 1$ for the models of multiple reflections discussed below. In Figures 3(b) and 3(c) we show how the total amount of Alfvén-wave reflection varies for different numbers of interfaces; i.e., in this case the Elsasser amplitude ratios are assumed to be equal to $\mathcal{R}_N^{1/2}$, for various values of N.

We compare the multiple-reflection model curves with the outputs of several different MHD turbulence simulations. Table 1 provides the base-10 logarithms of both Z_-/Z_+ and $\delta\rho/\rho_0$, extracted at various heliocentric distances in these simulations. Specifically, data points

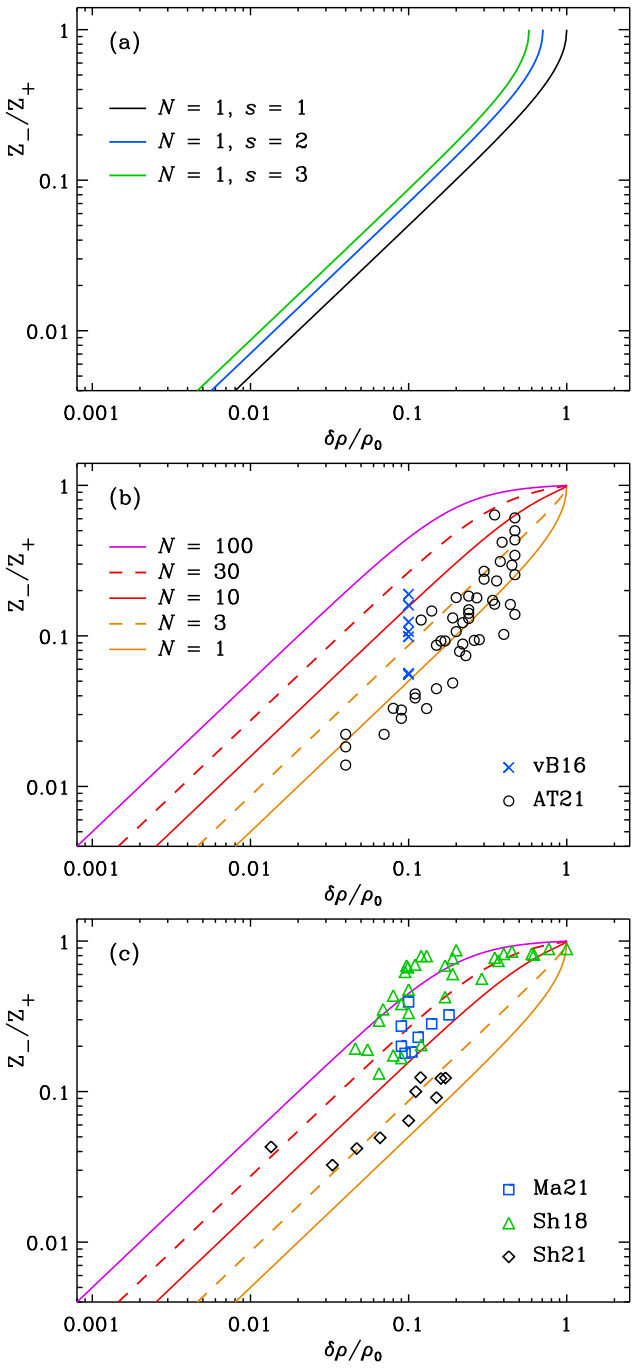

Figure 3. Degree of Alfvén-wave reflection, plotted as an amplitude ratio, as a function of a normalized rms density fluctuation. (a) For $N = 1$, we vary the shape factor $s = 1$ (black curve), $s = 2$ (blue curve), $s = 3$ (green curve). (b) For various values of N, we compare model results (see legend for curve colors and types) with data points extracted from numerical simulations. (c) Same as (b), but for different simulations. Reference abbreviations are vB16 (van Ballegooijen & Asgari-Targhi 2016), AT21 (Asgari-Targhi et al. 2021), Ma21 (Matsumoto 2021), Sh18 (Shoda et al. 2018), and Sh21 (Shoda et al. 2021).

from van Ballegooijen & Asgari-Targhi (2016) were extracted from their Figures 2(a) and 4(c), data points from Asgari-Targhi et al. (2021) were extracted from their Figures 4, 5, and 6, data points from Matsumoto (2021) were extracted from their Figures 2(c) and 2(d), data points from Shoda et al. (2018) were extracted from their Figures 2(a) and 2(b), and data points from Shoda et al. (2021) were extracted from their Figures 3 and 4 and Table 1.

For some of the simulations, Table 1 gives both the full Elsasser imbalance ratio (for the model containing the density fluctuations) as well as a minimum ratio corresponding to only wave reflection due to large-scale gradients in the smooth background atmosphere; the latter is denoted $(Z_-/Z_+)_0$ when it is given. To attempt to isolate the effect of the density fluctuations, the quantity plotted in Figure 3 is

$$\left(\frac{Z_-}{Z_+}\right)_{\rm eff} = \sqrt{\left(\frac{Z_-}{Z_+}\right)^2 - \left(\frac{Z_-}{Z_+}\right)_0^2}\,, \qquad (17)$$

but we also note that this is nearly always a very small correction. Plotting the full ratio would have produced noticeable changes in the data points shown in Figure 3(b) only for a few of the points with the lowest values of Z_-/Z_+.

Figure 3 shows some degree of agreement between the modeled trends and the simulated data. We note that no other significant correlations were found between the Elsasser amplitudes and other properties of the turbulence simulations (say, radial distance from the Sun or background magnetic field strength). The agreement seen in Figure 3 allows us to speculate about best-fitting values for N for each group of data points. To do this, we minimized a χ^2 difference between the base-10 logarithms of the simulated values of Z_-/Z_+ and a fine grid of model curves for different values of N. Because we are attempting to model long-time or ensemble averages of an instrinsically stochastic system, we allow for non-integer values of N.

For the combined vB16 and AT21 data in Figure 3(b), the best-fitting value of N was 1.32. Note that these simulations contain only incompressible Alfvénic fluctuations that propagate on a background with imposed density fluctuations. In general, an order-unity value of N may make sense because the eddies in strong MHD turbulence do not persist forever like sinusoidal wavetrains. They decay, often substantially, over just one to a few wavelengths or parallel correlation lengths (see, e.g., Zhou & Matthaeus 1990; Goldreich & Sridhar 1995; Schekochihin 2022). Thus, any given packet of Alfvénic turbulent energy may only live long enough to interact with one or two of our model density interfaces.

For the data in Figure 3(c), each group was treated separately. For Sh18, the best-fitting $N \approx 76.7$, for Ma21, the best-fitting $N \approx 21.5$, and for Sh21, the best-fitting $N \approx 3.38$. In contrast to the models shown in panel (b),

these models contain additional nonlinear sources of wave-like density fluctuations—such as those induced by the parametric decay instability—that propagate up and down relative to the Alfvén waves. Thus, one may expect to see a larger value of N than in the case of pure Alfvénic turbulence. Note that the largest effective values of N correspond to the one-dimensional models of Shoda et al. (2018), in which it has been suggested that wavetrains have longer lifetimes when not allowed to evolve in the directions transverse to the background magnetic field.

These results can be applied to future models of the solar wind that contain reflection-driven Alfvénic turbulence. Specifically, by defining a "floor" value of $\delta\rho/\rho_0$, below which we do not expect the solar wind to ever dip below, we could thus impose a corresponding floor on the Elsasser imbalance ratio. However, some caution is needed. For example, depending on the actual radial length-scales of the density fluctuations, there may only exist a finite number of effective interfaces between the Sun and some arbitrary radial distance r. Thus, it may not be appropriate to use the largest values of N found above (i.e., $N \approx 75$) because there may not be room for that many interfaces.

4. THE COMPLEX TRANSITION REGION

This paper's second application of the Stein (1971) reflection/transmission theory is to the sharp transition region (TR) between the Sun's chromosphere and corona. There have been multiple studies of how Alfvén waves are affected when they encounter this thin interface (e.g., Hollweg 1978, 1981; Wentzel 1978; Campos & Mendes 1995; Cranmer & van Ballegooijen 2005; Tsap & Kopylova 2021; Shoda & Takasao 2021). Many of these studies assumed a relatively simple geometry for the magnetic field that threads the TR. However, the properties of wave-mode conversion at a discontinuity depend sensitively on the magnetic-field angles α and β shown in Figure 1. Thus, our goal is to quantify the degree of wave reflection, transmission, and conversion for realistic ensembles of three-dimensional field-line geometries.

Before describing our model, though, we should note that numerical simulations of the chromosphere and corona sometimes have exhibited *shortfalls* of heating at the TR. For example, both Wang (1994) and Verdini et al. (2010) found that producing accurate models of the high-speed solar wind seemed to require both an extended source of heat—arising presumably from Alfvénic turbulence—and an additional (ad hoc) localized source of heat near the coronal base. Langangen et al. (2008) also found that adding an extra source of basal heating was required to understand observations of the on-disk counterparts of Type II spicules. Schiff & Cranmer (2016) were only able to model the thermodynamic properties of coronal "down-loops" (i.e., loops in which the temperature decreases toward the apex) by adding a heat source that behaves like an impulsive source of compressive MHD wave energy at the TR.

4.1. *Inputs Describing the Magnetic Carpet*

We make use of an existing set of Monte Carlo simulations of photospheric magnetic-flux transport and potential-field extrapolation into the low corona. Cranmer & van Ballegooijen (2010) developed these models initially to determine the rates at which closed field lines open up, and to estimate the rate of energy release by interchange reconnection in such events. Cranmer (2018) extended these models to predict the properties of reconnection-driven MHD waves. We continue to use these same models of the mixed-polarity "magnetic carpet," but we also note that more recent high-resolution data may point to the need for updating some parameters of these models (e.g., magnetic recycling times may be shorter; see Wiegelmann et al. 2013; Wang 2020).

Figure 4(a) shows a typical snapshot of the field-line geometry for one of these Monte Carlo simulations. The photospheric domain was assumed to be a square box 200 Mm on a side, and it was filled with point-like magnetic elements with positive and negative fluxes given by integer multiples of 10^{17} Mx. These models were evolved over several months of simulation time and have reached a dynamical steady state. The main free parameter is the large-scale magnetic flux imbalance fraction ξ, which is defined as the ratio of the net flux density $(|B_+| - |B_-|)$ to the absolute unsigned flux density $(|B_+| + |B_-|)$. Note that models with $\xi \lesssim 0.3$ are meant to simulate "balanced" patches of quiet Sun, whereas models with $\xi \gtrsim 0.7$ are meant to simulate more unipolar coronal-hole regions.

We compared the properties of 11 distinct Monte Carlo models with flux imbalance ratios $\xi = 0$, 0.1, 0.2, 0.3, 0.4, 0.5, 0.6, 0.7, 0.8, 0.9, and 0.99. For each, we extracted a large ensemble of 500,000 random samples for the field-line inclinations (i.e., values of α and β) at a typical transition-region height $z_{\rm TR} = 2.5$ Mm above the photosphere. The distributions of β azimuthal angles always appeared to be reasonably uniform. Figure 4(b) shows the cumulative distributions of values of $\cos\alpha$ for all 11 models. They appear somewhat isotropic, but slightly biased more towards horizontal orientations. Note that a truly isotropic distribution of field-line vectors would correspond to a straight line in Figure 4(b) ($y = x$) and thus would have a median value of $\cos\alpha = 0.5$, or a median angle $\alpha = 60^\circ$.

Figure 4(c) shows that the actual median values of $\cos\alpha$ take on values between 0.325 and 0.483 (i.e., corresponding to values of α between 71° and 61°, respectively), with large standard deviations. The most imbalanced ($\xi \geq 0.7$) configurations tend to have more vertically oriented fields than those

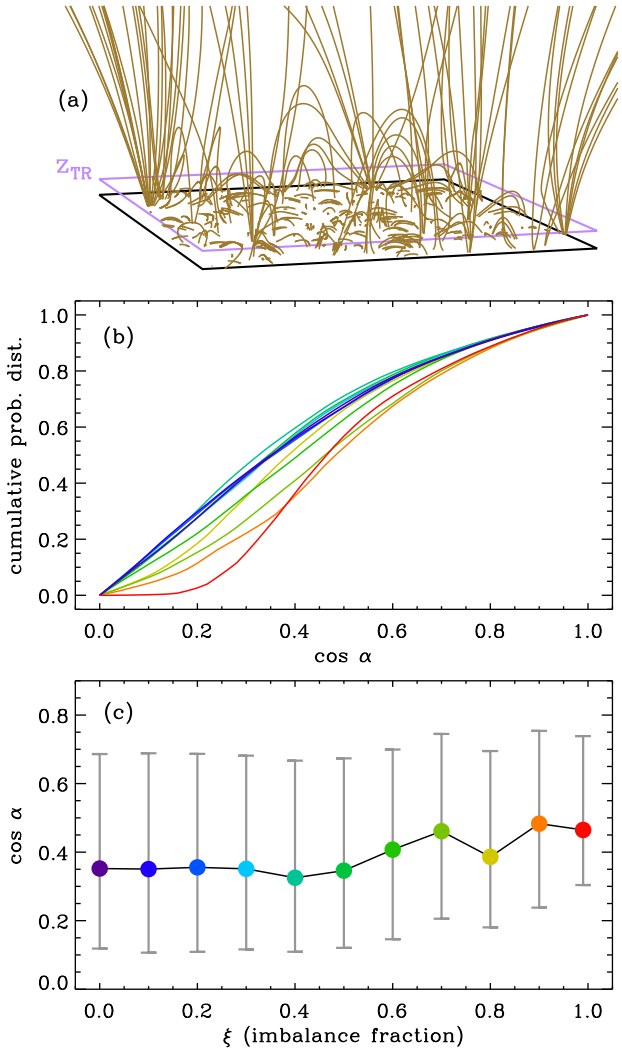

Figure 4. (a) Perspective rendering of field lines for an example timestep in the $\xi = 0.4$ model. The height of the TR is illustrated by the purple outline. (b) Cumulative probability distributions of $\cos\alpha$ for each of the 11 models. (c) Median (50% percentile) and ± 1 standard deviation limits (16% and 84% percentiles) for the distributions of $\cos\alpha$ for each value of ξ. Curve colors in (b) agree with symbol colors in (c).

with balanced fluxes, but the differences are subtle. However, the departures from vertical fields are important to consider, since an Alfvén wave incident at an interface with $\cos\alpha = 1$ (i.e., $\alpha = 0$) would produce no fast or slow magnetosonic waves in either reflection or transmission.

Each model run in a given Monte Carlo ensemble is constructed with randomly selected values of α and β, and these fully determine the direction of $\mathbf{B}_0$ at the interface. The β angles are sampled from a uniform distribution (between 0 and 360°), and the α angles are sampled from one of the distributions shown in Figure 4(b). The magnitude B_0 could also be sampled from observed or simulated distributions, but for simplicity we chose to select a single representative value to apply for each ensemble. Then, later we compare the results to other ensembles with different values of B_0. By varying the magnetic-field strength over several orders of magnitude between 0.1 and 1000 G, we can probe the behavior of TR-adjacent waves for the full range of quiet to active regions in the solar atmosphere.

For the purposes of the Stein (1971) interface model, we assume the gas pressure is constant across the TR, with

$$\frac{\rho_1}{\rho_2} = \frac{T_2}{T_1} = 30 \tag{18}$$

and the chromospheric values (on the side from which the incident wave comes) are $\rho_1 = 3 \times 10^{-14}$ g cm^{-3} and $T_1 = 10^4$ K. Note that typical quoted temperatures for the chromosphere (10^4 K) and corona (10^6 K) would presume the existence of a larger-magnitude jump of order $T_2/T_1 \approx 100$. However, the above value of 30 corresponds to only the lowest and steepest part of the TR that subtends no more than a few hundred km (see, e.g., Avrett & Loeser 2008). Because the temperature in the uppermost part of the TR rises more gradually, this region should not be counted as part of the sharp interface.

The final parameters to set, for each run in a Monte Carlo ensemble, are the frequency ω and wavenumber $\mathbf{k}$ of the incident Alfvén wave. Because the interface is assumed to be infinitely thin, the actual value of the wave frequency does not affect the calculation of reflection, transmission, and mode-coupling. To keep the values of all parameters realistic, we chose a representative value of $\omega = 0.02$ rad s^{-1}, corresponding to incident Alfvén-wave periods of about 5 minutes (see, e.g., Tomczyk et al. 2007). The wavenumber is specified by the dispersion relations and by θ_k, which we initially sample randomly between 0 and 180°. However, we accept or reject each trial value depending on the resulting value of Θ_{kB} for the incident Alfvén wave. We explore three distinct models of turbulent anisotropy that we define below:

1. Model I (isotropic): as long as $F_z > 0$ for the incident wave, all values of θ_k are retained.

2. Model S (slab): only values with $F_z > 0$ and $|\cos\Theta_{kB}| \geq 0.9848$ (i.e., quasi-parallel orientations of $\mathbf{k}$ within 10° of $\mathbf{B}_0$) are retained.

3. Model T (transverse): only values with $F_z > 0$ and $|\cos\Theta_{kB}| \leq 0.1736$ (i.e., $\mathbf{k}$ within 10° of the plane perpendicular to $\mathbf{B}_0$) are retained.

Note that despite many possible sampled values being rejected in models S and T, we keep resampling until the desired total number of trials is achieved.

In summary, each run in a given Monte Carlo ensemble involves sampling three variables from random distributions

(α, β, and θ_k) and keeping others fixed (e.g., ξ, B_0, ρ_2/ρ_1, T_2/T_1). Typically, each ensemble was constructed with 30,000 trials, using the Interactive Data Language's standard Mersenne Twister algorithm for pseudorandom number generation (Matsumoto & Nishimura 1998).

4.2. *Mode Coupling Results*

We begin by discussing the computed distributions of reflection and transmission coefficients (for all three types of MHD waves) for a typical Monte Carlo ensemble run with $B_0 = 10$ G, the distribution of $\cos\alpha$ angles taken from the $\xi = 0.7$ model, and an isotropic distribution of θ_k angles (i.e., Model I). The adopted value of the magnetic field corresponds to a plasma beta ratio (gas pressure to magnetic pressure) of about 0.01.

Figure 5(a) shows the computed distributions of $\mathcal{R}_{\rm AA}$ and $\mathcal{T}_{\rm AA}$ values, displaying reflection coefficients as negative values for the sake of clarity. In a majority of cases, the computed values are quite close to those predicted by Equation (8), i.e., $\mathcal{R}_{\rm AA} = 0.478$ and $\mathcal{T}_{\rm AA} = 0.522$, which were computed assuming $\beta = 0$. In fact, 69% of the 30,000 trials have a value of $\mathcal{R}_{\rm AA}$ that falls within 10% of its corresponding analytic value, and 67% of the trials have a value of $\mathcal{T}_{\rm AA}$ that falls within 10% of its analytic value. The remaining trials—amounting to roughly one-third of the total number—exhibit values that often indicate substantial coupling with the other modes.

Figures 5(b) and 5(c) show how the reflection and transmission coefficients of fast and slow magnetosonic waves behave as a function of the incident Alfvén wave's Θ_{kB} angle and the magnetic field's α angle. In the majority of cases, these four coefficients have quite small values, pointing to the relative weakness of mode coupling. We computed the total flux fractions going into non-Alfvénic modes, i.e.,

$$f = \mathcal{R}_{\rm FA} + \mathcal{T}_{\rm FA} + \mathcal{R}_{\rm SA} + \mathcal{T}_{\rm SA} \qquad (19)$$

and, although f sometimes grows to order unity, the median value of f (for the full distribution of 30,000 trials) was only 0.00081. Note also that incident waves propagating parallel to the magnetic field ($\cos\Theta_{kB} \approx 1$) tended to couple the most strongly to the fast mode, and incident waves propagating transversely to the field ($\cos\Theta_{kB} \approx 0$) coupled strongly to the slow mode. This behavior makes sense in the context of a low-plasma-beta environment, in which fast modes have similar phase speeds as Alfvén waves for nearly parallel propagation and slow modes have similar phase speeds as Alfvén waves for nearly perpendicular propagation. Matching phase speeds appears to be a necessary but not sufficient condition for strong mode coupling (see also Stein 1971; Vasquez 1990).

When considering the expected energy fluxes of upward and downward MHD waves that would be produced in the vicinity of the TR, we compute *mean values* for the reflection and transmission coefficients produced in each Monte Carlo ensemble. This is meant to be a proxy for some degree of spatial and temporal averaging over unresolved scales in the complex and rapidly evolving magnetic carpet. Thus, in the remainder of this section, we report only such mean values.

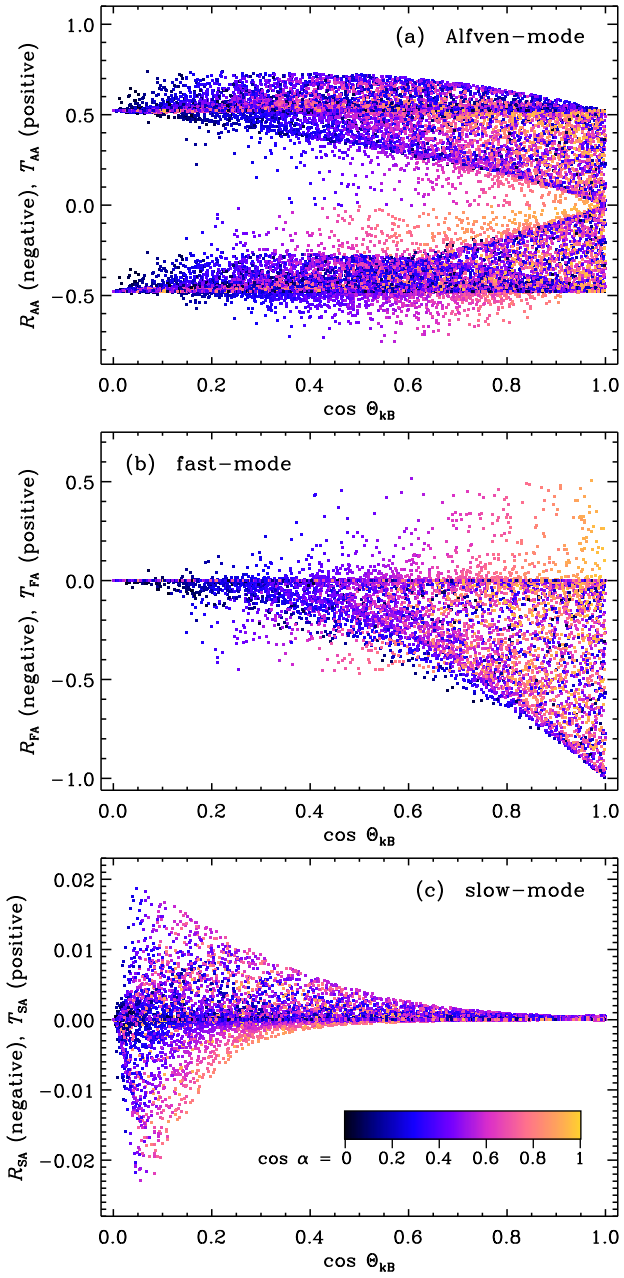

Figure 5. (a) Transmission (positive) and reflection (negative) coefficients for Alfvén waves produced at the TR for a Model-I Monte Carlo ensemble with $B_0 = 10$ G and $\xi = 0.7$. (b) Same as panel (a), but for fast-mode MHD waves. (c) Same as panel (a), but for slow-mode MHD waves. Symbol color denotes $\cos\alpha$, as shown in the color-bar.

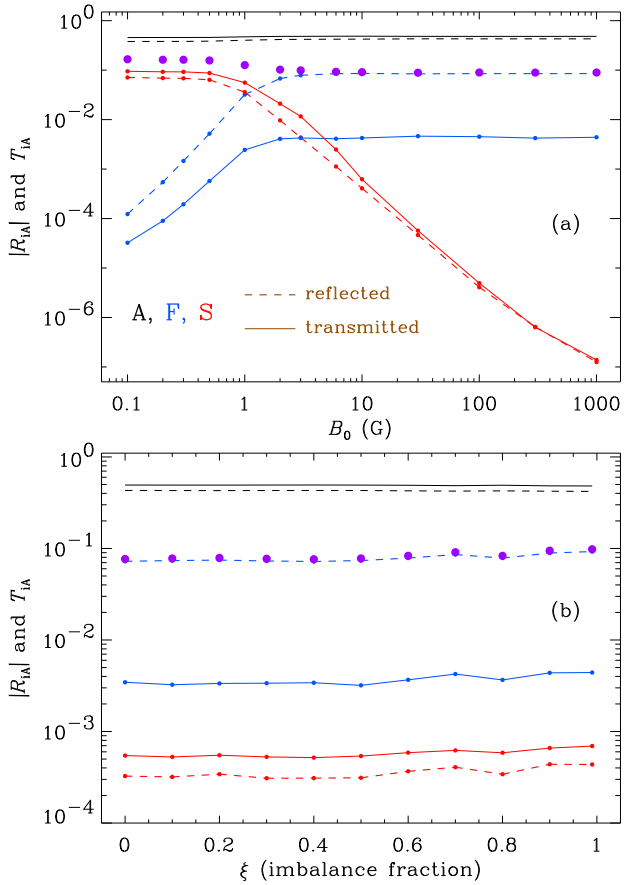

Figure 6. Ensemble-averaged reflection coefficients (dashed curves) and transmission coefficients (solid curves), with Alfvén, fast, and slow wave properties shown in black, blue, and red, respectively. (a) Dependence on B_0 for $\xi = 0.7$ and Model I. (b) Dependence on ξ for $B_0 = 10$ G and Model I. Values of f (i.e., totals for all four non-Alfvénic components) are shown with purple symbols.

Figure 6(a) shows how the mode-coupling coefficients behave as a function of B_0, for fixed choices of $\xi = 0.7$ and isotropic incident wavenumbers (Model I). As in the example above, for the strongest magnetic-field cases (i.e., the lowest plasma beta ratios) there is a much more efficient energy transfer from Alfvén to fast-mode waves than to slow-mode waves. This trend reverses itself for the weakest fields (i.e., highest plasma beta ratios), for which the coupling with slow-mode waves is most efficient. It is also interesting that there is always about an order of magnitude higher amount of reflection for fast-mode waves than transmission (i.e., $\mathcal{R}_{\rm FA}/\mathcal{T}_{\rm FA} \approx 10$), but the slow-mode waves seem to be partitioned more equally between the reflected and transmitted directions.

Figure 6(b) shows how the mean reflection and transmission coefficients vary as a function of ξ, for fixed values of $B_0 = 10$ G and isotropic incident wavenumbers (Model I).

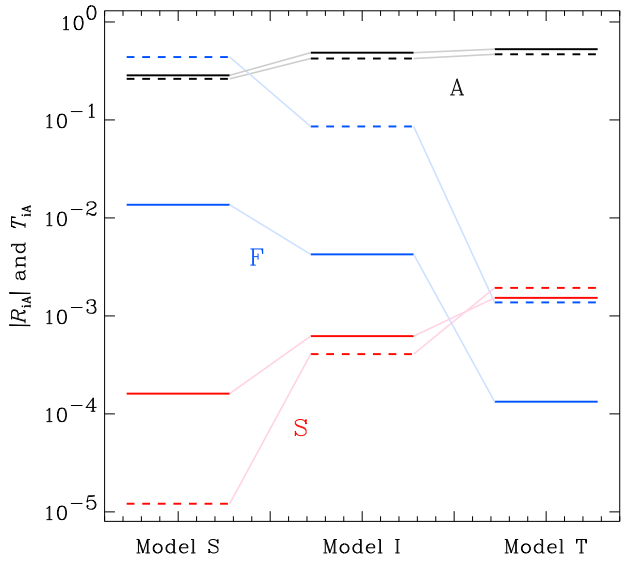

Figure 7. Ensemble-averaged reflection and transmission coefficients, with line styles and colors the same as in Figure 6. In order to illustrate the dependences on wavenumber anisotropy, we use dotted lines to connect identical parameters.

Varying ξ changes the probability distribution of $\cos\alpha$ values from which the Monte Carlo algorithm draws (see Figure 4(b)). It is somewhat surprising how little the mean coefficients change as one goes from balanced quiet-Sun patches ($\xi \approx 0$) to highly imbalanced coronal-hole regions ($\xi \approx 1$). It is possible, of course, that there exist other differences between these regions—such as differences in the mean height of the TR or different mean values of ρ or T—that would produce even larger variations in the reflection and transmission coefficients, had they been included.

Lastly, for the standard set of fixed parameters ($B_0 = 10$ G and $\xi = 0.7$), we vary the wavenumber anisotropy model and show the results in Figure 7. It makes sense that Model S produces the most intense coupling between Alfvén and fast-mode waves, since these two modes are the most similar to one another for parallel propagation (i.e., $\Theta_{kB} \to 0$). For the other extreme case of perpendicular propagation (Model T), the reflected fast-mode and slow-mode waves have roughly equal fluxes, and the transmitted slow-mode waves have about an order of magnitude larger flux than the transmitted fast-mode waves.

4.3. *Collisional Heating Rates*

In the solar atmosphere, all three types of MHD waves undergo dissipation due to particle-particle collisions (see, e.g., Alfvén 1947; Osterbrock 1961). The specific processes at work include thermal conductivity, viscosity, electrical resistivity (i.e., Ohmic or Joule dissipation), and a range of ion–neutral couplings. Both slow-mode and fast-mode magnetosonic waves tend to damp out more rapidly than do

Alfvén waves, which explains the popularity of the latter as proposed sources of energy deposition in the extended corona. However, our goal in this section is to simulate the dissipation of the newly produced slow-mode and fast-mode waves. This damping appears to produce a localized "bump" of heating in the vicinity of the TR that may be an important contributor to the overall coronal heating problem.

We compute the radial variation of wave energy density U_i, where the subscript i is either F or S for fast-mode or slow-mode waves, respectively. We use the time-steady wave-action conservation equation described by Cranmer & van Ballegooijen (2012), and for simplicity we provide it here only the limit of a negligibly small solar-wind speed (which is valid near the TR). Thus,

$$\frac{1}{A}\frac{d}{dr}\left(AV_{\mathrm{gr},i}U_i\right) \;=\; -2\gamma_i U_i \;\;, \qquad (20)$$

where A is the cross-sectional area of a presumed vertically oriented magnetic flux tube (i.e., $A \propto 1/B_0$), $V_{\mathrm{gr},i}$ is the group velocity of mode i, and γ_i is its total linear damping rate. We also define the total heating rate due to damping as $Q_i = 2\gamma_i U_i$. Since the above equation will be applied most often to the isotropic distribution of wavenumbers (Model I), we use the angle-averaging procedure described in Section 2.3 of Cranmer & van Ballegooijen (2012) to compute representative values of $V_{\mathrm{gr},i}$. Figure 8(a) shows how some of these quantities depend on height (measured as distance above the solar photosphere in units of the solar radius, $R_\odot$) in the vicinity of the TR. To set the background properties of the atmosphere, we chose the coronal-hole ZEPHYR model of Cranmer et al. (2007) that used a photospheric acoustic flux of 1 kW m^{-2}.

For a fully ionized plasma, the linear damping rates due to viscosity, thermal conduction, and Ohmic resistivity were discussed in detail by, e.g., Braginskii (1965) and Whang (1997). We use the specific forms given in Appendix B of Cranmer & van Ballegooijen (2012), which include modification terms for weak collisions. These were derived in order to avoid the "molasses limit" of the classical expressions; i.e., an unphysical divergence of the transport coefficients when the mean time between collisions becomes infinite (see also Williams 1995). However, for a plasma that is only partially ionized, the presence of neutral atoms produces additional resistivity via Pedersen currents (Goodman 2004, 2011; Kazeminezhad & Goodman 2006). This effect must be included when modeling the chromosphere and TR. Thus, the modified version of the total damping rate is given by the sum of viscous, Ohmic, and conductive terms,

$$\gamma_i \;=\; \gamma_{\mathrm{vis},i} + \gamma_{\mathrm{ohm},i}(1+\Gamma) + \gamma_{\mathrm{con},i} \;\;. \qquad (21)$$

Note that the conductive damping term $\gamma_{\mathrm{con},i}$ is identically zero for the purely incompressible Alfvén mode, but it is a non-negligible contributor to the total damping rate for the fast and slow mode waves. The Pedersen correction term Γ, due to the presence of neutrals, is discussed in more detail by Kazeminezhad & Goodman (2006) and is given by

$$\Gamma \;=\; \left(\frac{\rho_{\mathrm{HI}}}{\rho_{\mathrm{H}}}\right)^2 \frac{\Omega_e \Omega_p}{\nu_e^* \nu_p^*} \qquad (22)$$

where Ω_p and Ω_e are the cyclotron frequencies of electrons and protons, and ν_e^* and ν_p^* are the reduced collision frequencies defined by Goodman (2004). We specify the neutral hydrogen density fraction $\rho_{\mathrm{HI}}/\rho_{\mathrm{H}}$ with the same temperature-dependent tabulation that was used by Cranmer et al. (2007), which has a similar behavior as more realistic time-dependent models (e.g., Carlsson et al. 2016; Przybylski et al. 2022).

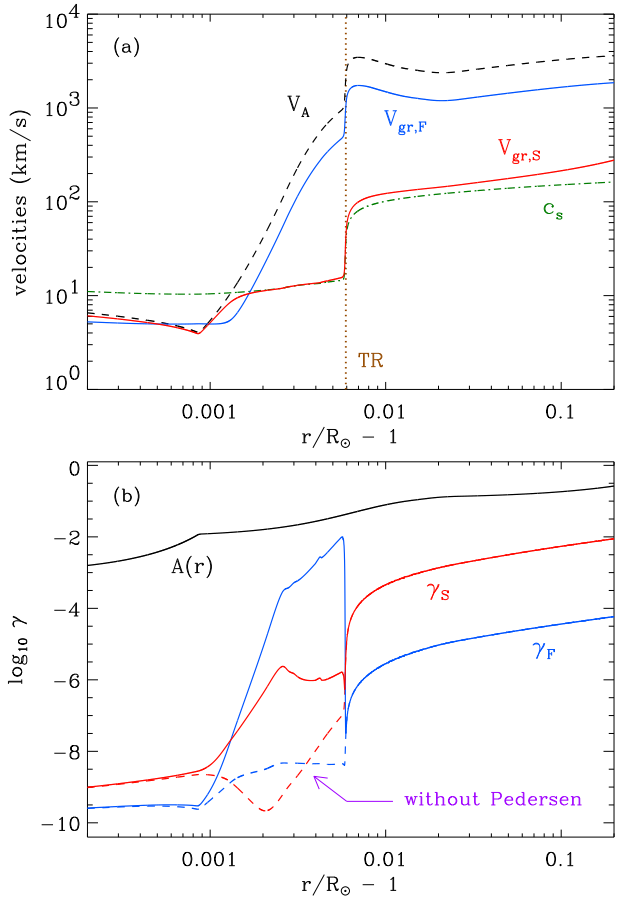

Figure 8. (a) Radial dependence of characteristic velocities such as the sound speed c_s (green dot-dashed curve), Alfvén speed V_A (black dashed curve), and angle-averaged group velocities for fast-mode (blue solid curve) and slow-mode (red solid curve) waves. (b) Radial dependence of flux-tube area A (black solid curve) and collisional damping rates for fast-mode (blue) and slow-mode (red) waves, with both total values computed with Pedersen conductivity (solid curves) as well as the fully-ionized Braginskii limit (dashed curves).

Figure 8(b) shows the resulting height dependence of $\gamma_{\rm F}$ and $\gamma_{\rm S}$, both with and without the inclusion of the Pedersen term. We find, as expected, that $\Gamma \ll 1$ in the corona, but there is a strong enhancement in both damping rates (due to $\Gamma \gg 1$) in the upper chromosphere. Note that the damping rates also depend on the square of the wavenumber, so there is an associated dependence on the wave frequency. As above, we chose a typical value of $\omega = 0.02$ rad s^{-1}, corresponding to a period of 5 minutes, and we discuss the dependence on ω further below.

In order to solve Equation (20) both above and below the TR, there are several additional quantities to specify. We are assuming that mode coupling produces the "new" fast-mode and slow-mode waves precisely at the TR interface. Thus, we must use the transmission coefficients to determine the boundary conditions on U_i for integrating upwards, and we must use the reflection coefficients to determine the boundary conditions on U_i for integrating downwards. The interface is defined as the location at which the time-steady model temperature $T(r)$ is equal to $(T_1 T_2)^{1/2} = 5.48 \times 10^4$ K, and for this model it is found at a height $r_{\rm TR}$ of 0.0059 $R_\odot$ (i.e., 4,100 km) above the photospheric base. The incident Alfvén wave is assumed to have a known vertical energy flux $F_{z,{\rm A}}$ at the interface, and various observational constraints have provided values of this quantity in the range of roughly 3–6 kW m^{-2} (Cranmer & van Ballegooijen 2005, 2012). We choose the lower bound of that range (3 kW m^{-2}) so as not to overestimate the heating-rate predictions of this paper. Using this value, the boundary conditions for the fluxes of transmitted and reflected magnetosonic waves are given as either $F_{z,i} = F_{z,{\rm A}} \mathcal{T}_{i{\rm A}}$ (for upward waves) or $F_{z,i} = F_{z,{\rm A}} \mathcal{R}_{i{\rm A}}$ (for downward waves), and the energy densities are given as

$$U_i = F_{z,i} / V_{{\rm gr},i} \tag{23}$$

which we solve four times (for fast and slow modes; in the upward and downward directions) at the interface.

4.4. *Localized Heating Results*

Equation (20) was solved numerically by integrating both upwards and downwards from the TR. Because of the sharp gradients in this region, we found that straightforward finite-difference integration steps were often unstable, even with very finely spaced grids in radial distance. Thus, we took advantage of the form of the differential equation and noted that it can be written as

$$\frac{dy}{y} = -\frac{dr}{H} \tag{24}$$

where $y = A V_{{\rm gr},i} U_i$ and $H = V_{{\rm gr},i} / 2\gamma_i$. This equation has a known solution for $H \approx$ constant, so a reasonably robust finite-differencing scheme, going from step (n) to step $(n+1)$, was found to be

$$y^{(n+1)} = y^{(n)} \exp\left(-\frac{r^{(n+1)} - r^{(n)}}{H^{(n)}} \right) . \tag{25}$$

Once $y(r)$ is determined, we compute $U_i(r)$ for each mode, as well as the corresponding rms velocity amplitudes $\delta v_i = (U_i/\rho)^{1/2}$. This expression makes use of the fact that linear MHD waves carry exactly half of their total fluctuation energy in the form of kinetic energy (see, e.g., Goedbloed & Poedts 2004).

Figure 9(a) shows the computed radial dependences of wave velocity amplitudes for the typical case shown in Figure 5; i.e., $B_0 = 10$ G, $\xi = 0.7$, and an isotropic distribution of θ_k angles (Model I). We show both the full solutions for slow-mode and fast-mode amplitudes and also those computed without any damping (i.e., assuming $\gamma_i = 0$). Note that the upward slow-mode waves become very strongly damped in the corona, whereas the downward slow-mode waves experience almost no damping (with the damped amplitudes only decreasing to 0.997 times the undamped amplitudes). The downward fast-mode waves have the largest amplitudes of the four magnetosonic waves generated at the TR, and they are also damped rather weakly (only down to 0.98 times the corresponding undamped amplitudes). Also shown are the transverse velocity amplitudes of incompressible Alfvénic waves that are computed self-consistently by the time-steady ZEPHYR model of Cranmer et al. (2007). These rms amplitudes account for fluctuations in both dimensions transverse to the vertical magnetic field. Thus, the values of $\sim$50 km s^{-1} in the low corona correspond to projected nonthermal line widths of order $50/\sqrt{2} \approx 35$ km s^{-1}, which agrees with off-limb measurements (e.g., Banerjee et al. 1998).

The corresponding heating rates Q_i, expressed in units of μW m^{-3}, are shown in Figure 9(b). Despite the relatively weak damping for the downward fast-mode waves, they contribute the most to the heating due to their large amplitudes. In fact, it is this component that is most responsible for the compact "bump" of extra heating due to newly produced waves at the TR interface. For the model parameters shown here, the peak of the bump exceeds the background heating—due Alfvénic turbulence in the ZEPHYR model—by about a factor of five. This extra heating has been computed without concern for how it would self-consistently alter the presume background plasma state. Given that the extra heating occurs *below* the modeled TR, we anticipate that including it in the time-steady energy balance would *lower* the height of the TR. This may help explain why prior generations of the ZEPHYR code (Cranmer et al. 2007, 2013) found the TR to occur at heights substantially above those seen in observationally guided models (e.g., Fontenla et al. 1990; Avrett & Loeser 2008).

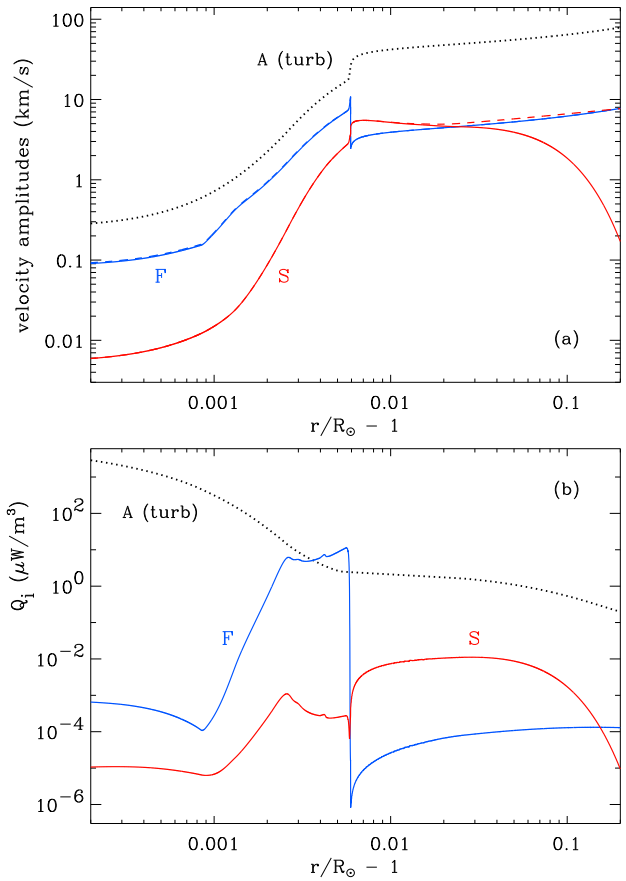

Figure 9. (a) Radial dependence of wave velocity amplitudes for fast-mode waves (blue curves), slow-mode waves (red curves), and Alfvénic turbulence from the time-steady model (black dotted curve). For magnetosonic modes, both undamped (dashed) and damped (solid) amplitudes are shown. (b) Radial dependence of volumetric heating rates due to fast-mode waves (blue curves), slow-mode waves (red curves), and Alfvénic turbulence (black dotted curve).

Figure 10 shows how the peak value of Q_i depends on B_0. Here, we continue to assume $\xi = 0.7$ and the wavenumber anisotropy properties of Model I, as in Figure 6(a). Heating due to newly produced magnetosonic waves at the TR remains dominated by downward-propagating fast-mode waves for field strengths exceeding just a few Gauss. In regions with even weaker fields, the peak heating rate is driven mainly by the damping of both upward and downward slow-mode waves. The vertical struts show how the model with $B_0 = 10$ G exhibits either stronger or weaker heating when the wavenumber anisotropy conditions are varied to Models S and T (see also Figure 7). Most notably, the assumption that most of the upflowing Alfvén waves have wavenumbers nearly parallel to the magnetic field (i.e., Model S) seems to produce a peak heating rate at the TR that is about 25 times larger than the expected level of background heating from

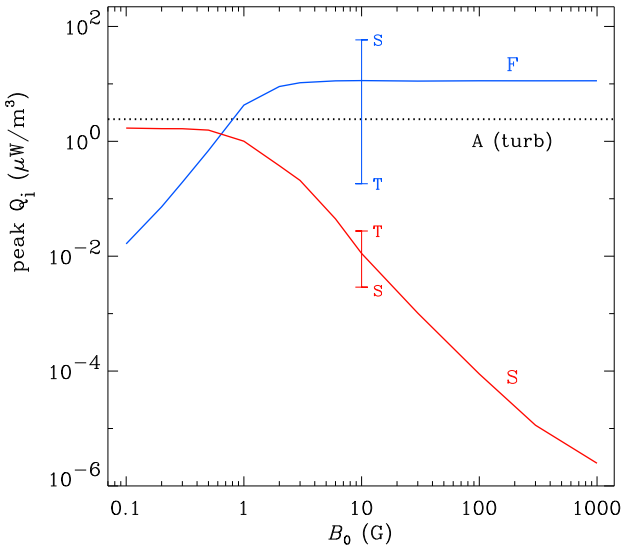

Figure 10. Peak heating rates due to the damping of fast-mode waves (blue curve) and slow-mode waves (red curve), produced at the TR, as a function of B_0 for $\xi = 0.7$ and Model I. Vertical struts at $B_0 = 10$ G show how the peak heating rate changes when other wavenumber anisotropy models are applied (Models S or T). The typical heating rate due to incompressible Alfvénic turbulence at the TR is also shown (black dotted curve).

incompressible turbulence. (In a completely self-consistent model, the heating due to Alfvénic turbulence would vary with B_0 as well, but here we treat this as an aspect of the "background" atmosphere.)

As mentioned above, the collisional heating rate Q_i is proportional to the square of the assumed wave frequency. When varying ω up and down by several orders of magnitude from the baseline value of 0.02 rad s^{-1}, we found that the radial profile of $Q_i(r)$ simply shifted up and down by the expected amount and did not display any noticeable changes in shape. However, our assumption of a single monochromatic frequency is not likely to be realistic. The Sun appears to exhibit continuous power spectra of wave energy flux as a function of frequency. If this flux spectrum is a power-law with $P \propto \omega^{-n}$, then the spectrum of associated heating rates would go as $Q \propto \omega^{2-n}$, and its integral over frequency would behave as ω^{3-n}. Thus, if $n > 3$ the total heating would be dominated by the low-frequency end of the spectrum, and if $n < 3$ it would be dominated by the high-frequency end of the spectrum. Unfortunately, observations of both chromospheric and coronal waves do not show a consensus, with reported values of the power-law slopes varying between 1 and 4 for different regions and diagnostics (see, e.g., Reardon et al. 2008; Tomczyk & McIntosh 2009; Molnar et al. 2021, 2023).

For the models with $B_0 \gtrsim 3$ G discussed above (i.e., the cases where the heating is dominated by downward-

propagating fast-mode waves), the following scaling relation provides a good way to estimate the peak heating rate at the TR:

$$\max(Q_{\rm F}) \approx \frac{F_{z,{\rm A}}\langle \mathcal{R}_{\rm FA}\rangle}{\lambda_{\rm eff}} \left(\frac{5\ {\rm min}}{\mathcal{P}}\right)^2 , \qquad (26)$$

where $\mathcal{P}$ is the wave period, $\langle \mathcal{R}_{\rm FA}\rangle$ is the ensemble-averaged reflection coefficient for fast-mode waves, and we define an effective length scale $\lambda_{\rm eff} = 0.034\,R_\odot$ to set the overall normalization. Other models of the background plasma and ionization state will exhibit different values of $\lambda_{\rm eff}$, but the other scalings given above should remain valid.

5. DISCUSSION AND CONCLUSIONS

In this paper we have explored a few of the possible ramifications of Alfvén waves in the solar atmosphere encountering sharp discontinuities in density. In Section 3, we found that linear reflection from multiple interfaces may help explain simulated enhancements in sunward-propagating Alfvénic turbulence in the presence of density fluctuations. Over the past decade, it has been realized that purely incompressible reflection-driven turbulence may not be sufficient to heat the extended corona and accelerate the solar wind on its own (e.g., van Ballegooijen & Asgari-Targhi 2016). Without compressible effects, the inward-to-outward Elsasser amplitude ratio Z_-/Z_+ may not exceed values of order 0.01. However, there is a great deal of observational evidence for density fluctuations with magnitudes $\delta\rho/\rho_0$ exceeding 0.1 in the corona and solar wind (Issautier et al. 1998; Spangler 2002; Miyamoto et al. 2014; Hahn et al. 2018; Wexler et al. 2019; Mohan 2021; Cuesta et al. 2023). The associated reflection due to these fluctuations may enhance the total amount of Alfvénic reflection to values of order $Z_-/Z_+ \gtrsim 0.1$ (see Figure 3). Those more intense levels of sunward-propagating waves are much more likely to provide sufficient levels of turbulent heating for the corona and solar wind.

In Section 4, we found that taking account of a realistic distribution of magnetic field directions (i.e., the highly structured "magnetic carpet") may allow upward-propagating Alfvén waves to convert a non-negligible fraction of their energy into both fast-mode and slow-mode MHD waves at the sharp TR. These newly produced waves dissipate efficiently in the vicinity of the TR and produce a narrow peak of heating that, in some cases, may exceed the dominant rate of turbulent heating by an order of magnitude. These little bumps of extra heating are not likely to be responsible for the majority of chromospheric or coronal heating, but their existence should not be ignored. In fact, this heretofore unknown source of heating may be an explanation for why some models have not been able to produce realistic coronal temperature distributions without adding sharp (but essentially ad-hoc) sources of heat at this location (e.g., Wang 1994; Langangen et al. 2008; Verdini et al. 2010; Schiff & Cranmer 2016).

It is important to note that our prediction of a narrow bump of additional heating at the TR is not based on a fully self-consistent simulation. A more comprehensive understanding of this effect will require taking into account some additional processes and complexities, such as the following.

1. More realistic geometrical parameters for the system should be adopted. This includes the use of self-consistent distributions of magnetic-field directions and magnitudes—say, from simulations like Bifrost (Carlsson et al. 2016; Molnar 2022)—and also a naturally "corrugated" TR interface between the chromosphere and corona (Feldman et al. 1979; Peter 2013). It may also be useful to separate the closed and open magnetic field lines to study differences in wave propagation between these two regions.

2. If the Alfvén waves coming from below are already turbulent by the time they reach the TR (and many simulations show they are; see van Ballegooijen et al. 2011), then their wavenumber angles θ_k should be sampled from a probability distribution that is consistent with the behavior of anisotropic MHD turbulent cascade.

3. The physics of wave dissipation likely needs to be treated in a more comprehensive manner. Besides Pedersen currents, several other channels of ion-neutral interaction have been proposed to be important in the chromosphere (e.g., Khomenko et al. 2018; Martínez-Sykora et al. 2020). Also, the collisional transport coefficients may also be higher if the electrons, ions, and neutral atoms have non-Maxwellian velocity distributions (Husidic et al. 2021). Lastly, our assumption of a simple temperature-dependent ionization-recombination equilibrium, which includes only hydrogen, should be replaced by more self-consistent physics (again, see codes like Bifrost or MuRAM; Carlsson et al. 2016; Przybylski et al. 2022).

4. This work assumed that the only waves incident to the TR interface were Alfvén waves coming up from below. Of course, the real wave ecosystem of the solar atmosphere must also involve magnetosonic waves coming up from below (e.g., Osterbrock 1961; de Wijn et al. 2009; Jess et al. 2023) as well as coronal fluctuations that propagate downwards (as we discussed in Section 3). The near-Sun solar wind is observed to contain all three types of linear MHD waves, as well as other compressive fluctuations that are not normal modes of a homogeneous plasma (e.g., Tu & Marsch 1994; Zhao et al. 2021). We still do not

know to what extent these waves come from the solar surface or are generated in situ.

This paper has examined several solar applications of Stein's (1971) theory of MHD-wave interactions at a sharp interface, and there are several others that could be explored as well. For example, closed loops in the low corona contain two TRs, one at each footpoint, and their finite length is known to produce resonances (Ionson 1978; Nakariakov & Verwichte 2005) and "sloshing oscillations" (Xia et al. 2022). The seemingly infinite regress of multiple reflections and transmissions from Section 3 may be extended to better understand the behavior of trapped waves in these loops. Further out in the open-field corona and solar wind, there exist a wide range of field-aligned density striations (Raymond et al. 2014; DeForest et al. 2016). Magyar & Van Doorsselaere (2022) suggested that interactions between Alfvén waves and these striations may result in the production of a $1/f$ power spectrum of turbulent fluctuations, which is seen at low frequencies in the solar wind. Treating these striations as sharp interfaces may lead to new insights about how they affect MHD waves in various environments.

The authors gratefully acknowledge Bernie Vasquez and Munehito Shoda for many valuable discussions. The authors are also grateful to the anonymous referee for many constructive suggestions that have improved this paper. This work was supported by the National Aeronautics and Space Administration (NASA) under grant 80NSSC20K1319, and by the National Science Foundation (NSF) under grant 1613207. The National Center for Atmospheric Research is a major facility sponsored by the NSF under Cooperative Agreement No. 1852977. M.E.M. was supported by the George Ellery Hale Graduate Student Fellowship at the University of Colorado Boulder. This research made extensive use of NASA's Astrophysics Data System (ADS).

REFERENCES

Alfvén, H. 1947, MNRAS, 107, 211 [ADS]

Anderson, E., Bai, Z., Bischof, C., et al. 1999, LAPACK Users' Guide, 3rd ed. (Philadelphia: SIAM) [DOI]

Aschwanden, M. J. 2006, Physics of the Solar Corona: An Introduction with Problems and Solutions, 2nd ed. (Berlin: Springer) [ADS]

Asgari-Targhi, M., Asgari-Targhi, A. Hahn, M., & Savin, D. W. 2021, ApJ, 911, 63 [ADS]

Avrett, E. H., & Loeser, R. 2008, ApJS, 175, 229 [ADS]

Axford, W. I., & McKenzie, J. F. 1992, in Solar Wind Seven, ed. E. Marsch & R. Schwenn (New York: Pergamon), 1 [ADS]

Bacchini, F., Pucci, F., Malara, F., & Lapenta, G. 2022, PhRvL, 128, 025101 [ADS]

Banerjee, D., Teriaca, L., Doyle, J. G., & Wilhelm, K. 1998, A&A, 339, 208 [ADS]

Bavassano, B., Dobrowolny, M., & Moreno, G. 1978, SoPh, 57, 445 [ADS]

Bogdan, T. J., Rosenthal, C. S., Carlsson, M., et al. 2002, Astron. Nachr., 323, 196 [ADS]

Braginskii, S. I. 1965, Rev. Plasma Phys., 1, 205 [ADS]

Cally, P. S. 2022, MNRAS, 510, 1093 [ADS]

Cally, P. S., & Goossens, M. 2008, SoPh, 251, 251 [ADS]

Campos, L. M. B. C., & Mendes, P. M. V. M. 1995, MNRAS, 276, 1041 [ADS]

Carlsson, M., Hansteen, V. H., Gudiksen, B. V., Leenaarts, J., & De Pontieu, B. 2016, A&A, 585, A4 [ADS]

Cranmer, S. R. 2018, ApJ, 862, 6 [ADS]

Cranmer, S. R., & van Ballegooijen, A. A. 2005, ApJS, 156, 265 [ADS]

Cranmer, S. R., & van Ballegooijen, A. A. 2010, ApJ, 720, 824 [ADS]

Cranmer, S. R., & van Ballegooijen, A. A. 2012, ApJ, 754, 92 [ADS]

Cranmer, S. R., van Ballegooijen, A. A., & Edgar, R. J. 2007, ApJS, 171, 520 [ADS]

Cranmer, S. R., van Ballegooijen, A. A., & Woolsey, L. N. 2013, ApJ, 767, 125 [ADS]

Cranmer, S. R., & Woolsey, L. N. 2015, ApJ, 812, 71 [ADS]

Cuesta, M. E., Chhiber, R., Fu, X., et al. 2023, ApJL, 949, L19 [ADS]

DeForest, C. E., Matthaeus, W. H., Viall, N. M., & Cranmer, S. R. 2016, ApJ, 828, 66 ADS.

De Pontieu, B., Martens, P. C. H., & Hudson, H. S. 2001, ApJ, 558, 859 [ADS]

de Wijn, A. G., McIntosh, S. W., & De Pontieu, B. 2009, ApJL, 702, L168 [ADS]

Elsasser, W. M. 1950, Phys. Rev., 79, 183 [ADS]

Feldman, U., Doschek, G. A., & Mariska, J. T. 1979, ApJ, 229, 369 [ADS]

Fletcher, L., Cargill, P. J., Antiochos, S. K., & Gudiksen, B. V. 2015, SSRv,188, 211 [ADS]

Fontenla, J. M., Avrett, E. H., & Loeser, R. 1990, ApJ, 355, 700 [ADS]

Goedbloed, J. P. H., & Poedts, S. 2004, Principles of Magnetohydrodynamics (Cambridge: Cambridge Univ. Press) [ADS]

Goldreich, P., & Sridhar, S. 1995, ApJ, 438, 763 [ADS]

Goodman, M. L. 2004, A&A, 416, 1159 [ADS]

Goodman, M. L. 2011, ApJ, 735, 45 [ADS]
Goossens, M. L., Arregui, I., & Van Doorsselaere, T. 2019, Frontiers Astron. Space Sci., 6, 20 [ADS]
Hahn, M., D'Huys, E., & Savin, D. W. 2018, ApJ, 860, 34 [ADS]
Hasan, S. S., Kalkofen, W., van Ballegooijen, A. A., & Ulmschneider, P. 2003, ApJ, 585, 1138 [ADS]
Hollweg, J. V. 1978, SoPh, 56, 305 [ADS]
Hollweg, J. V. 1981, SoPh, 70, 25 [ADS]
Hollweg, J. V. 1984, SoPh, 91, 269 [ADS]
Hollweg, J. V. 1990, Comput. Phys. Rep., 12, 205 [ADS]
Hollweg, J. V., & Kaghashvili, E. K. 2012, ApJ, 744, 114 [ADS]
Huang, Z., Shi, C., Sioulas, N., & Velli, M. 2022, ApJ, 935, 60 [ADS]
Husidic, E., Lazar, M., Fichtner, H., Scherer, K., & Poedts, S. 2021, A&A, 654, A99 [ADS]
Ionson, J. A. 1978, ApJ, 226, 650 [ADS]
Issautier, K., Meyer-Vernet, N., Moncuquet, M., & Hoang, S. 1998, J. Geophys. Res., 103, 1969 [ADS]
Jess, D. B., Jafarzadeh, S., Keys, P. H., et al. 2023, Living Rev. Solar Phys., 20, 1 [ADS]
Kaghashvili, E. K. 1999, ApJ, 512, 969 [ADS]
Kaghashvili, E. K. 2007, Phys. Plasmas, 14, 044502 [ADS]
Kaghashvili, E. K. 2013, J. Plasma Phys., 79, 797 [ADS]
Kazeminezhad, F., & Goodman, M. L. 2006, ApJS, 166, 613 [ADS]
Khomenko, E., Vitas, N., Collados, M., & de Vicente, A. 2018, A&A, 618, A87 [ADS]
Kigure, H., Takahashi, K., Shibata, K., et al. 2010, PASJ, 62, 993 [ADS]
Langangen, Ø., De Pontieu, B., Carlsson, M., et al. 2008, ApJL, 679, L167 [ADS]
Lee, M. A., & Roberts, B. 1986, ApJ, 301, 430 [ADS]
Li, H.-S.,, & Zweibel, E. G. 1987, ApJ, 322, 248 [ADS]
Lou, Y. Q., & Rosner, R. 1986, ApJ, 309, 874 [ADS]
Lynch, B. J., Edmondson, J. K., & Li, Y. 2014, SoPh, 289, 3043 [ADS]
Magyar, N., & Van Doorsselaere, T. 2022, ApJ, 938, 98 [ADS]
Martínez-Sykora, J., Leenaarts, J., De Pontieu, B., et al. 2020, ApJ, 889, 95 [ADS]
Matsumoto, M., & Nishimura, T. 1998, ACM Trans. Mod. Comput. Simul., 8, 3 [DOI]
Matsumoto, T. 2021, MNRAS, 500, 4779 [ADS]
McDougall, A. M. D., & Hood, A. W. 2007, SoPh, 246, 259 [ADS]
Miyamoto, M., Imamura, T., Tokumaru, M., et al. 2014, ApJ, 797, 51 [ADS]
Mohan, A. 2021, A&A, 655, A77 [ADS]
Molnar, M. E. 2022, PhD Dissertation, Department of Astrophysical and Planetary Sciences, University of Colorado Boulder [ADS]
Molnar, M. E., Reardon, K. P., Cranmer, S. R., Kowalski, A. F., Chai, Y. & Gary, D. 2021, ApJ, 920, 125 [ADS]
Molnar, M. E., Reardon, K. P., Cranmer, S. R., Kowalski, A. F., & Milić, I. 2023, ApJ, 945, 154 [ADS]
Morton, R. J., Sharma, R., Tajfirouze, E., & Miriyala, H. 2023, Rev. Mod. Plasma Phys., 7, 17 [ADS]
Murawski, K., Nakariakov, V. M., & Pelinovsky, E. N. 2001, A&A, 366, 306 [ADS]
Musielak, Z. E., & Ulmschneider, P. 2002, A&A, 386, 606 [ADS]
Nakariakov, V. M., Roberts, B., & Murawski, K. 1998, A&A, 332, 795 [ADS]
Nakariakov, V. M., & Verwichte, E. 2005, Living Rev. Solar Phys., 2, 3 [ADS]
Osterbrock, D. E. 1961, ApJ, 134, 347 [ADS]
Parnell, C. E., & De Moortel, I. 2012, Phil. Trans. Roy. Soc. A, 370, 3217 [ADS]
Peter, H. 2013, SoPh, 288, 531 [ADS]
Przybylski, D., Cameron, R., Solanki, S. K., et al. 2022, A&A, 664, A91 [ADS]
Raymond, J. C., McCauley, P. I., Cranmer, S. R., & Downs, C. 2014, ApJ, 788, 152 [ADS]
Reardon, K. P., Lepreti, F., Carbone, V., & Vecchio, A. 2008, ApJL, 683, L207 [ADS]
Ryutova, M., & Hagenaar, H. 2007, SoPh, 246, 281 [ADS]
Schekochihin, A. A. 2022, J. Plasma Phys., 88, 155880501 [ADS]
Schiff, A. J., & Cranmer, S. R. 2016, ApJ, 831, 10 [ADS]
Shoda, M., Chandran, B. D. G., & Cranmer, S. R. 2021, ApJ, 915, 52 [ADS]
Shoda, M., & Takasao, S. 2021, A&A, 656, A111 [ADS]
Shoda, M., Yokoyama, T., & Suzuki, T. K. 2018, ApJ, 853, 190 [ADS]
Snow, B., Fedun, V., Gent, F. A., Verth, G., & Erdélyi, R. 2018, ApJ, 857, 125 [ADS]
Spangler, S. R. 2002, ApJ, 576, 997 [ADS]
Spruit, H. C. 1981, A&A, 98, 155 [ADS]
Srivastava, A. K., Ballester, J. L., Cally, P. S., et al. 2021, J. Geophys. Res., 126, e2020JA029097 [ADS]
Stein, R. F. 1971, ApJS, 22, 419 [ADS]
Tarr, L. A., Linton, M., & Leake, J. 2017, ApJ, 837, 94 [ADS]
Terradas, J., Andries, J., & Verwichte, E. 2011, A&A, 527, A132 [ADS]
Tomczyk, S., & McIntosh, S. W. 2009, ApJ, 697, 1384 [ADS]
Tomczyk, S., McIntosh, S. W., Keil, S. L., et al. 2007, Science, 317, 1192 [ADS]
Tsap, Y., & Kopylova, Y. 2021, SoPh, 296, 5 [ADS]
Tu, C.-Y., & Marsch, E. 1994, J. Geophys. Res., 99, 21481 [ADS]
Turing, A. M. 1948, Q. J. Mechanics Appl. Math., 1, 287 [DOI]
Valley, G. C. 1971, ApJ, 168, 251 [ADS]
Valley, G. C. 1974, ApJ, 188, 181 [ADS]

van Ballegooijen, A. A., & Asgari-Targhi, M. 2016, ApJ, 821, 106 [ADS]

van Ballegooijen, A. A., & Asgari-Targhi, M. 2017, ApJ, 835, 10 [ADS]

van Ballegooijen, A. A., Asgari-Targhi, M., Cranmer, S. R., & DeLuca, E. 2011, ApJ, 736, 3 [ADS]

Van Doorsselaere, T., Srivastava, A. K., Antolin, P., et al. 2020, SSRv, 216, 140 [ADS]

Vasquez, B. J. 1990, ApJ, 356, 693 [ADS]

Vasquez, B. J., & Hollweg, J. V. 1996, J. Geophys. Res., 101, 13527 [ADS]

Verdini, A., Velli, M., Matthaeus, W. H., Oughton, S., & Dmitruk, P. 2010, ApJL, 708, L116 [ADS]

Vickers, E., Ballai, I., & Erdélyi, R. 2018, SoPh, 293, 139 [ADS]

Wang, Y.-M. 1994, ApJL, 435, L153 [ADS]

Wang, Y.-M. 2020, ApJ, 904, 199 [ADS]

Wentzel, D. G. 1978, SoPh, 58, 307 [ADS]

Wexler, D. B., Hollweg, J. V., Efimov, A. I., et al. 2019, ApJ, 871, 202 [ADS]

Whang, Y. C. 1997, ApJ, 485, 389 [ADS]

Wiegelmann, T., Solanki, S. K., Borrero, J. M., et al. 2013, SoPh, 283, 253 [ADS]

Williams, L. L. 1995, ApJ, 453, 953 [ADS]

Xia, F., Wang, T., Su, Y., Zhao, J., Zhang, Q., Veronig, A. M., & Gan, W. 2022, ApJL, 936, L13 [ADS]

Yuan, D., Pascoe, D. J., Nakariakov, V. M., Li. B., & Keppens, R. 2015, ApJ, 799, 221 [ADS]

Zhao, S. Q., Yan, H., Liu, T. Z., Liu, M., & Shi, M. 2021, ApJ, 923, 253 [ADS]

Zhou, Y., & Matthaeus, W. H. 1990, J. Geophys. Res., 95, 14881 [ADS]

Table 1. Turbulence Reflection Rates and Density Fluctuations from Published MHD Simulations

$r/R_\odot$	$\log(Z_-/Z_+)$	$\log(Z_-/Z_+)_0$	$\log(\delta\rho/\rho_0)$	Source
1.5	–1.2314	–1.7175	–1.0000	vB16
2.4	–1.2098	–1.6048	–1.0000	vB16
3.6	–0.9674	–1.8117	–1.0000	vB16
5.5	–1.0028	–1.9588	–1.0000	vB16
8.4	–0.9067	–2.0498	–1.0000	vB16
13.0	–0.7228	–2.0853	–1.0000	vB16
20.0	–0.7958	–2.0816	–1.0000	vB16
2.0	–1.4367	–1.6351	–1.0458	AT21, Fig. 4(a,b)
4.0	–0.9061	–1.6842	–0.6576	AT21, Fig. 4(a,b)
10.0	–0.7341	–1.7724	–0.6198	AT21, Fig. 4(a,b)
20.0	–0.7434	–1.7570	–0.6990	AT21, Fig. 4(a,b)
2.0	–1.5607	–1.6243	–1.3979	AT21, Fig. 4(d,e)
4.0	–0.8451	–1.6690	–0.6198	AT21, Fig. 4(d,e)
10.0	–0.5699	–1.7103	–0.5229	AT21, Fig. 4(d,e)
20.0	–0.8893	–1.6920	–0.9208	AT21, Fig. 4(d,e)
2.0	–1.4881	–1.6243	–1.1549	AT21, Fig. 4(g,h)
4.0	–0.7443	–1.6651	–0.5686	AT21, Fig. 4(g,h)
10.0	–0.3774	–1.6105	–0.4089	AT21, Fig. 4(g,h)
20.0	–0.8293	–1.6320	–0.8539	AT21, Fig. 4(g,h)
2.0	–0.9788	–1.6243	–0.3979	AT21, Fig. 4(j,k)
4.0	–0.4638	–1.6021	–0.3279	AT21, Fig. 4(j,k)
10.0	–0.2156	–1.4809	–0.3279	AT21, Fig. 4(j,k)
20.0	–0.1963	–1.5431	–0.4559	AT21, Fig. 4(j,k)
2.0	–1.3233	–1.6243	–0.9586	AT21, Fig. 5(a,b)
4.0	–1.0492	–1.6690	–0.8239	AT21, Fig. 5(a,b)
10.0	–0.8239	–1.8182	–0.6198	AT21, Fig. 5(a,b)
20.0	–0.8808	–1.7804	–0.6198	AT21, Fig. 5(a,b)
2.0	–1.5229	–1.6243	–1.3979	AT21, Fig. 5(d,e)
4.0	–1.0231	–1.6842	–0.7959	AT21, Fig. 5(d,e)
10.0	–0.6223	–1.7626	–0.5229	AT21, Fig. 5(d,e)
20.0	–1.0256	–1.7447	–0.7696	AT21, Fig. 5(d,e)
2.0	–1.3979	–1.6243	–1.0458	AT21, Fig. 5(g,h)
4.0	–0.9629	–1.6690	–0.6990	AT21, Fig. 5(g,h)
10.0	–0.5051	–1.7212	–0.4202	AT21, Fig. 5(g,h)
20.0	–0.8751	–1.6778	–0.7212	AT21, Fig. 5(g,h)
2.0	–0.8507	–1.6133	–0.3279	AT21, Fig. 5(j,k)
4.0	–0.6320	–1.5740	–0.4437	AT21, Fig. 5(j,k)
10.0	–0.3010	–1.5963	–0.3279	AT21, Fig. 5(j,k)

Table 1 *continued*

Table 1 *(continued)*

$r/R_\odot$	$\log(Z_-/Z_+)$	$\log(Z_-/Z_+)_0$	$\log(\delta\rho/\rho_0)$	Source
20.0	–0.3617	–1.5624	–0.3279	AT21, Fig. 5(j,k)
2.0	–1.3413	–1.6189	–0.9586	AT21, Fig. 6(a,b)
4.0	–1.0872	–1.6612	–0.6778	AT21, Fig. 6(a,b)
10.0	–1.1220	–1.8094	–0.6383	AT21, Fig. 6(a,b)
20.0	–1.2900	–1.7917	–0.7212	AT21, Fig. 6(a,b)
2.0	–1.4881	–1.6243	–1.3979	AT21, Fig. 6(d,e)
4.0	–1.0414	–1.6612	–0.6576	AT21, Fig. 6(d,e)
10.0	–1.0189	–1.7913	–0.5528	AT21, Fig. 6(d,e)
20.0	–1.4337	–1.7804	–0.8861	AT21, Fig. 6(d,e)
2.0	–1.3869	–1.6133	–1.0969	AT21, Fig. 6(g,h)
4.0	–1.0170	–1.6368	–0.5850	AT21, Fig. 6(g,h)
10.0	–0.7867	–1.7320	–0.4559	AT21, Fig. 6(g,h)
20.0	–1.3144	–1.7192	–0.8239	AT21, Fig. 6(g,h)
2.0	–0.7855	–1.5786	–0.3565	AT21, Fig. 6(j,k)
4.0	–0.5898	–1.4649	–0.3279	AT21, Fig. 6(j,k)
10.0	–0.5283	–1.5506	–0.3468	AT21, Fig. 6(j,k)
20.0	–0.7570	–1.5017	–0.4685	AT21, Fig. 6(j,k)
1.06	–0.7373	—	–0.9788	Ma21
1.1	–0.7460	—	–1.0223	Ma21
1.4	–0.6990	—	–1.0458	Ma21
2.0	–0.6394	—	–0.9393	Ma21
3.0	–0.5500	—	–0.8539	Ma21
5.0	–0.4903	—	–0.7447	Ma21
11.0	–0.4044	—	–1.0000	Ma21
21.0	–0.5654	—	–1.0458	Ma21
1.04	–0.4179	—	–1.0458	Sh18, $\lambda_0 = 0.01$ Mm
1.1	–0.5287	—	–1.1871	Sh18, $\lambda_0 = 0.01$ Mm
1.3	–0.7144	—	–1.3372	Sh18, $\lambda_0 = 0.01$ Mm
2.0	–0.8794	—	–1.1871	Sh18, $\lambda_0 = 0.01$ Mm
4.0	–0.7773	—	–1.0458	Sh18, $\lambda_0 = 0.01$ Mm
11.0	–0.6904	—	–0.9208	Sh18, $\lambda_0 = 0.01$ Mm
31.0	–0.7595	—	–1.0969	Sh18, $\lambda_0 = 0.01$ Mm
101.0	–0.7212	—	–1.2596	Sh18, $\lambda_0 = 0.01$ Mm
1.04	–0.3224	—	–1.0000	Sh18, $\lambda_0 = 0.1$ Mm
1.1	–0.3625	—	–1.0969	Sh18, $\lambda_0 = 0.1$ Mm
1.3	–0.4535	—	–1.1612	Sh18, $\lambda_0 = 0.1$ Mm
2.0	–0.4776	—	–1.0000	Sh18, $\lambda_0 = 0.1$ Mm
4.0	–0.3726	—	–0.7696	Sh18, $\lambda_0 = 0.1$ Mm
11.0	–0.2503	—	–0.5376	Sh18, $\lambda_0 = 0.1$ Mm
31.0	–0.2190	—	–0.7212	Sh18, $\lambda_0 = 0.1$ Mm
101.0	–0.2048	—	–1.0223	Sh18, $\lambda_0 = 0.1$ Mm

Table 1 *continued*

Table 1 *(continued)*

$r/R_\odot$	$\log(Z_-/Z_+)$	$\log(Z_-/Z_+)_0$	$\log(\delta\rho/\rho_0)$	Source
1.04	–0.1574	—	–0.9586	Sh18, $\lambda_0 = 1$ Mm
1.1	–0.1630	—	–1.0132	Sh18, $\lambda_0 = 1$ Mm
1.3	–0.1739	—	–1.0044	Sh18, $\lambda_0 = 1$ Mm
2.0	–0.1637	—	–0.7696	Sh18, $\lambda_0 = 1$ Mm
4.0	–0.1314	—	–0.4318	Sh18, $\lambda_0 = 1$ Mm
11.0	–0.0857	—	–0.2218	Sh18, $\lambda_0 = 1$ Mm
31.0	–0.0857	—	–0.3979	Sh18, $\lambda_0 = 1$ Mm
101.0	–0.0610	—	–0.6990	Sh18, $\lambda_0 = 1$ Mm
1.04	–0.0996	—	–0.8861	Sh18, $\lambda_0 = 10$ Mm
1.1	–0.0996	—	–0.9208	Sh18, $\lambda_0 = 10$ Mm
1.3	–0.1146	—	–0.7212	Sh18, $\lambda_0 = 10$ Mm
2.0	–0.1107	—	–0.4559	Sh18, $\lambda_0 = 10$ Mm
4.0	–0.0904	—	–0.2076	Sh18, $\lambda_0 = 10$ Mm
11.0	–0.0526	—	0.0000	Sh18, $\lambda_0 = 10$ Mm
31.0	–0.0526	—	–0.1135	Sh18, $\lambda_0 = 10$ Mm
101.0	–0.0701	—	–0.3468	Sh18, $\lambda_0 = 10$ Mm
1.05	–1.3671	—	–1.8697	Sh21
2.0	–1.4881	—	–1.4815	Sh21
2.54	–1.3777	—	–1.3279	Sh21
3.0	–1.3064	—	–1.1805	Sh21
3.7	–1.1928	—	–1.0000	Sh21
5.0	–1.0394	—	–0.8239	Sh21
10.0	–0.9092	—	–0.7670	Sh21
20.0	–0.9126	—	–0.7959	Sh21
30.0	–0.9062	—	–0.9245	Sh21
39.5	–1.0000	—	–0.9547	Sh21